11th International Symposium on Turbulence and Shear Flow Phenomena (TSFP11)
Southampton, UK, July 30 to August 2, 2019

SPATIALLY SAMPLED MEASUREMENTS OF ATMOSPHERIC TURBULENCE USING UNMANNED AERIAL VEHICLES

Caleb A. Canter and Sean C. C. Bailey
Department of Mechanical Engineering
University of Kentucky
Lexington, Kentucky 40506, USA
caleb.canter@uky.edu; sean.bailey@uky.edu

ABSTRACT

This paper provides an overview of recently conducted experiments in which atmospheric boundary layer turbulence was measured by unmanned aerial vehicles. These experiments were conducted as part of the large-scale "Lower Atmospheric Process Studies at Elevation - a Remotely-piloted Aircraft Team Experiment (LAPSE-RATE)" measurement campaign held in Colorado's San Luis Valley. Two types of measurements are examined, the first type is focused on measuring profiles of thermodynamic properties for atmospheric boundary layer investigations. Profiles of temperature, wind velocity, and turbulent kinetic energy measured during a morning transition from stable to convective conditions were examined for altitudes up to 900 m above ground level. The second measurement type utilizes long transect flights over nearly homogeneous terrain to spatially measure turbulence statistics. Energy spectra and velocity structure functions up to 10th order were examined and the scaling of the structure function exponents compared to those measured from prior studies.

INTRODUCTION

To understand turbulent phenomena, obtaining a spatial description of the structure and organization of the turbulence is of primary theoretical interest, particularly in the form of wavenumber spectra and spatial correlations. However, in spatially resolved atmospheric boundary layer (ABL) measurements the spatial resolution is relatively poor (i.e. through LIDAR measurements whose resolution is typically 10s of meters) relative to the Kolmogorov scale (on the order of millimeters). Turbulence data is therefore frequently obtained in the form of temporal information through cup and sonic anemometers, which themselves only have temporal response of only 1-2 Hz and 20 Hz respectively and spatial resolution of 10s of centimeters.

The use of small unmanned aerial systems (sUAS) for atmospheric boundary layer research has been growing rapidly, Egger *et al.* (2002); Hobbs *et al.* (2002); Spiess *et al.* (2007); van den Kroonenberg *et al.* (2008); Martin *et al.* (2014); Elston *et al.* (2015); Wildmann *et al.* (2015); Platis *et al.* (2016); Lampert *et al.* (2016). van den Kroonenberg *et al.* (2008); Martin *et al.* (2014); Elston *et al.* (2015); Wildmann *et al.* (2015); Platis *et al.* (2016); Lampert *et al.* (2016).and introduce new possibilities for obtaining a spatial description of the structure and organization of turbulence. This is due to the ability of a sUAS to spatially sample the flow field, which results in reduced reliance on Taylor's flow hypothesis (Taylor, 1938) and increased statistical convergence due to collecting substantially more data than a fixed-point measurement in the same time period. Finally, a UAV also has an advantage over fixed towers in terms of portability and the potential to measure in locations where construction of a tower is prohibitive.

Here we present results from data collected as part of the Lower Atmospheric Process Studies at Elevation - a Remotely-piloted Aircraft Team Experiment (LAPSE-RATE). LAPSE-RATE took place in Colorados San Luis Valley between 14-19 July, 2018, and was organized in conjunction with the International Society for Atmospheric Research using Remotely-piloted Aircraft (ISARRA). This activity included participation by a variety of university, government and industry teams. Over the course of six days, over 100 participants supported the coordinated deployment of 50 different unmanned aircraft to complete 1287 total flights, accumulating 262.4 flight hours. These flights were conducted under both FAA Certificates of Authorization (COAs) and FAA Part 107, with the COAs generally supporting flights up to altitudes of 3000 feet above ground level. In addition to the aerial assets, a variety of ground-based observational assets were deployed. These included the Collaborative Lower Atmospheric Mobile Profiling System (CLAMPS; Reference), two Doppler Lidar systems, numerous radiosondes, and mobile surface instrumentation associated with vehicles and small towers. Finally, forecasting and modeling support was provided by the National Weather Service forecast office in Pueblo, CO and the National Center for Atmospheric Research.

Specifically, for this paper we present results from two different flight trajectories intended to acquire different types of information. The first trajectory was designed for the measurement of vertical profiles of thermodynamics variables up to heights up to 900 m. The second flight trajectory targeted the spatial sampling of turbulence at a constant height. For these flights, the aircraft flew straight line transects of approximately 13,000 m allowing the measurement of turbulence over 3 decades of wavenumber range.

EXPERIMENT DESCRIPTION

The aircraft used for the turbulence measurements were built around a Skywalker X8 airframe, significantly modified for unmanned operations (see Figure 1). Each UAV was equipped with a five-hole pressure probe sys-

Figure 1. Modified Skywalker X8 airframe used for turbulence measurements.

tem, measuring the local velocity vector relative to the aircraft. The on-board instrumentation included the five-hole probe, pressure transducers, a data acquisition unit (DAQ), and an on-board personal computer as well as pressure, temperature and humidity sensors. The pressure from the five-hole probe was referenced to the static pressure measured by a separate Pitot-static tube used by the autopilot for airspeed sensing. The velocity of the probe relative to the ground is determined via an on-board inertial measurement unit (IMU) and global positioning system (GPS). Post-processing of the five-hole probe data is implemented by subtracting the measured probe translational and rotational velocity vectors from the measured velocity signal, leaving only the wind velocity vectors. Details are provided in Witte *et al.* (2017).

Flight speeds were approximately an order of magnitude higher than the local wind speed, resulting in spatially sampled wind, temperature, pressure, and humidity measurements. Data was acquired at 200 Hz, although frequency response of the five-hole probe was found to have a 3dB cutoff frequency of 60 Hz, as determined by measuring the probe system's (i.e. probe, tubing and transducer) response to a step change in pressure. This corresponds to a resolved sample approximately every 0.3 m. The pressure, temperature and humidity sensors had much slower response, resulting in an independent sample every 20 m.

Additional reference measurements were made using a stationary 2.1 m tower, measuring the surface energy balance, including air and soil temperature and humidity, ground heat flux, wind speed and direction, sensible and latent heat fluxes, and solar radiation. However, these results are not included here for brevity.

The measurements were conducted in the San Luis Valley located in Colorado, USA. The terrain in the valley is flat farmland with minimal crop growth present during the measurement campaign. Two flight trajectories are considered here. The first trajectory targeted measurements of vertical gradients of atmospheric properties, and consisted of measurements made on continual spiraling ascents and descents up to heights of 900 m above ground level (AGL). Here we present results from July 18 2018, composed of data from five flights flown hourly from a location near the center of the valley, near Center, CO at 37°38'42.8"N 105°55'41.9"W. The individual flights initiated at 7:15 MDT, 9:15 MDT, 10:15 MDT, 11:15 MDT and 11:45 MDT.

The second flight trajectory consisted of straight line transects at 100 m AGL. The flights initiated at Leech Airfield located at the center of the valley and proceeded 13,000 m due east at 20 m/s, before conducting a 180 degree turn and return flight to Leech airfield. All flights were performed under Federal Aviation Authority Part 107 operating rules, with the aircraft kept within line of sight of the

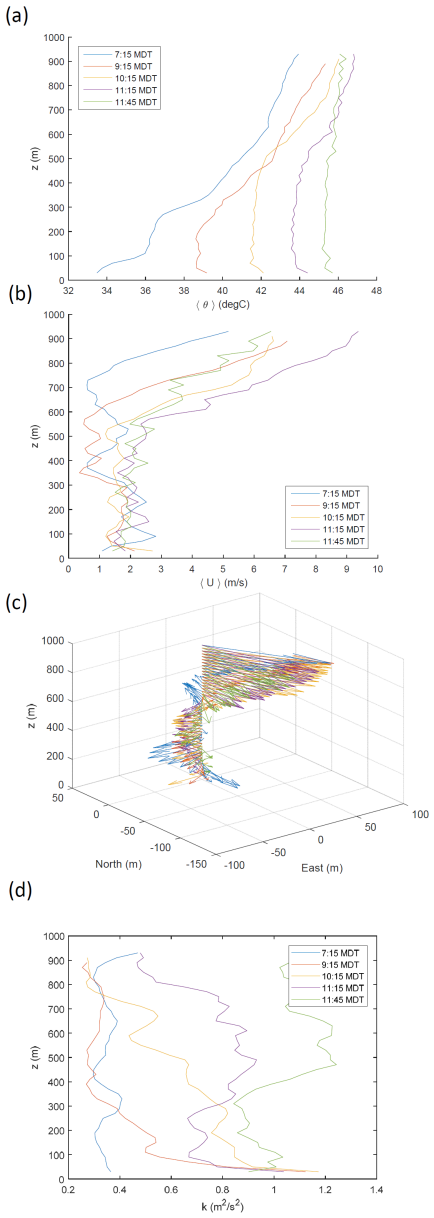

Figure 2. Vertical profiles of (a) potential temperature; (b) horizontal component of velocity; (c) wind direction vector; and (d) turbulent kinetic energy per unit mass.

operator using two ground chase vehicles. The lead vehicle was used to provide advance warning of any unexpected road conditions which may have required cessation of operations. The second vehicle contained the pilot, and observer and maintained visual contact with the aircraft at all times. The first two flights were performed in well-mixed convective boundary layer conditions (initiating at 12:48 MDT and 15:51 MDT on July 16, 2018) with the the third flight taking place in transitioning boundary layer conditions on July 17, 2018, initiating at 9:04 MDT. Ambient weather was mostly clear with scattered clouds for both flight days.

RESULTS

As an example of the results from the profile flights, Figure 2(a) shows the evolution of the profile of average potential temperature, $\langle\theta\rangle$, illustrating the transition from sta-

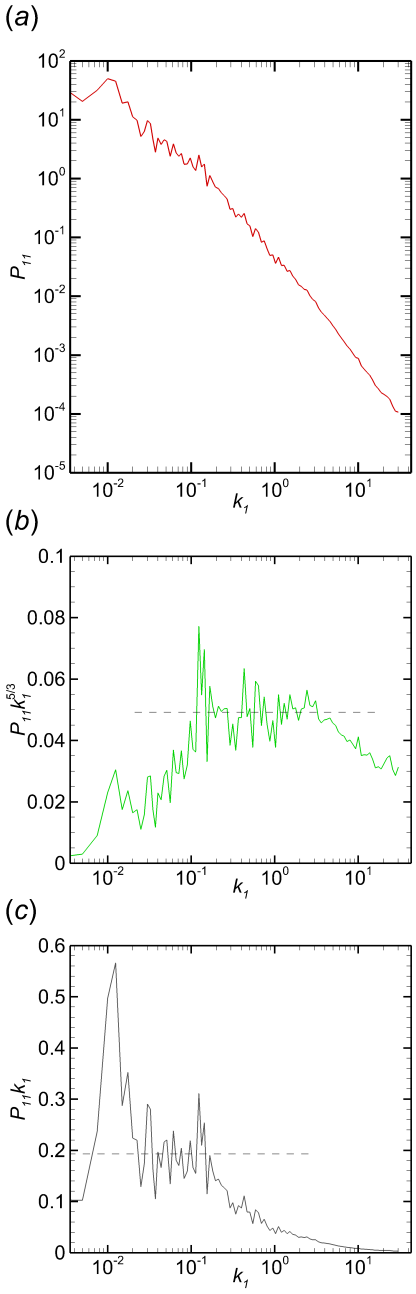

Figure 3. Longitudinal wavenumber spectrum of veloicity measured during long transect flight presented in (a) traditional log-log form; (b) scaled to illustrate the inertial subrange; and (c) scaled to illustrated k_1^{-1} scaling.

ble conditions to fully mixed-layer conditions between 7:15 MDT and 11:45 MDT. This figure also highlights the corresponding boundary layer growth from 100 m at 7:15 MDT to 200 m, 500 m, 600 m and $>$ 1000 m by 11:45 MDT. Figure 2(b) shows corresponding average horizontal wind velocity magnitude profiles. Worth noting is the existence of a strong wind shear above 500 m, persisting throughout the measurements and unconnected to the atmospheric boundary layer growth due to its relationship to upper level winds coming over the neighboring mountains. Velocity vectors calculated from the average velocity at each altitude, shown in Figure 2(c), illustrate how the wind shear also exists in direction, as well as magnitude. In addition, is evidence of the veering wind direction under stable conditions, which become disrupted by the turbulent transport which develops during the transition to mixed layer conditions. This turbulent transport is quantified in the profiles of turbulent kinetic energy per unit mass, k, shown in Figure 2(d), which highlight the growth of the turbulence within the mixed layer as the morning progresses. The profiles show relatively low k throughout the measurement domain at 7:15 MDT, but as the insolation increases over the morning, the turbulent kinetic energy develops near the surface and eventually permeates the full measurement domain by 11:45 MDT. These results, which are typical for different measurement days, and across multiple locations in the valley, highlight the complex, non-canonical atmospheric boundary layer transition process which occurred due to the presence of the surrounding topography, specifically the cold-air drainage out of the higher altitudes during the early morning hours, followed by the warm air outflow as the surface temperature increases and the atmospheric boundary layer transitions to convective conditions.

Although the vertical profiles show a highly layered structure, profiles measured across the valley indicated that in the horizontal plane, the conditions were spatially homogeneous. To take advantage of this homogeneity, long transect flights were conducted to spatially measure the turbulence statistics. As an example of the results obtained from these transect flights, Figure 3 shows the longitudinal energy spectrum calculated from the 9:04 MDT flight. Here, the Cartesian coordinates have been aligned such that the u_1,x_1 direction is along the flight path, and the corresponding longitudinal spectrum calculated in the wavenumber domain. Note that, since the sample spacing from the flight data is dependent on the ground speed which can vary both spatially and temporally, prior to calculating the Fourier transform, the velocity signal was first re-sampled onto a regularly spaced interval in the x_1 direction. The Fourier transform could then be calculated in wavenumber, k_1, space.

The un-scaled spectrum, shown in Figure 3(a) shows that a wavenumber range spanning four decades was measured during this flight. As shown in Figure 3(b), which presents the same spectrum pre-multiplied by $k_1^{5/3}$, roughly 1.5 decades of inertial subrange was also measured. Note that the slope of this inertial subrange does not appear to exactly correspond to -5/3 slope, as expected and addressed later. Note also that the roll-off at high wavenumbers appears to be due to probe response and suggests that the unity gain response of this particular probe is closer to 10 Hz, as the 60 Hz measured in the laboratory is the 3dB cutoff frequency. The low wavenumber bound of the inertial subrange appears to be characterized by a k_1^{-1}-scaled region, as shown in Figure 3(c) which shows the same spectrum pre-multiplied by k_1. Although there is still significant scatter observed in these results, they do provide strong support for the overlap arguments of, for example Townsend (1976) and Perry *et al.* (1986). Note, however, that the conditions of these particular flights were not strictly neutrally buoyant, and some caution must be exercised when assessing turbulent boundary layer theory under these conditions.

To assess the scaling of the inertial subrange, the mean dissipation rate, ε, and Kolmogorov length scale, η must first be determined. To do so we employ the third order structure function

$$S_{xx}^3 = \langle (u_1(x_1 - x_0) - u_1(x_0))^3 \rangle \qquad (1)$$

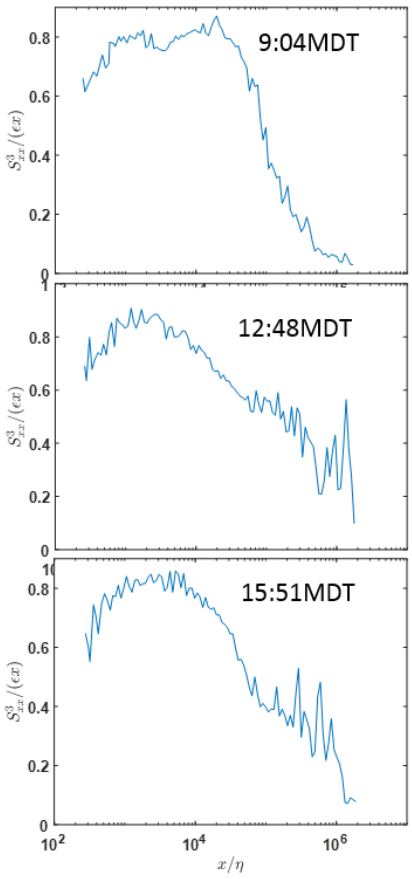

Figure 4. Ensemble-averaged third order structure function calculated for each flight.

where u_1 is the velocity component aligned with the flight path, x_1 is the spatial position in the flight direction, position x_0 is a reference position, and $\langle\rangle$ indicates an ensemble average. Following Kolmogorov (1941), the mean dissipation rate can then be determined from

$$\varepsilon = -\frac{S^3_{xx}}{0.8x} \tag{2}$$

within the inertial subrange, where $x = x_1 - x_0$ being the longitudinal separation. With ε known, the Kolmogorov scale can then be determined from $\eta = (\nu^3/\varepsilon)^{1/4}$.

The third order structure function was calculated for each 1500 m segment of the flight profile and ensemble averaged to produce the results shown in Figure 4. These results have been scaled such that a constant value of 0.8 will occur in the inertial subrange. For the transitioning boundary layer, there is a clear plateau, consistent with an inertial subrange between $x = 10^3\eta$ and $x = 10^4\eta$, indicating at least a decade of inertial subrange was captured in this flight. For the mixed layer conditions, due to the enhanced energy content at larger scales, the inertial subrange was not as well captured, with less of a plateau evident. Note that the poor frequency response of the five-hole probe used results in the roll-off observed at smaller spatial separations. Based on the limited evidence of the inertial range for the mixed-layer conditions, we limit further analysis to the transitioning boundary layer case.

The reduced reliance on Taylor's hypothesis, combined with the high Reynolds number turbulence of the atmospheric boundary layer, produces an opportunity to examine the scaling of the higher order structure functions

$$S^n_{xx} = \langle (u_1(x) - u_1(x_0))^n \rangle \tag{3}$$

where n is the order of the structure functions and x being the longitudinal separation $x_1 - x_0$. Within the inertial subrange, the structure functions are expected to follow a power law and scale with the dissipation rate such that

$$S^n_{xx} = A_n(\varepsilon x)^{\zeta_n} \tag{4}$$

where ζ_n is the scaling exponent, predicted by Kolmogorov (1941) to follow $\zeta_n = n/3$. As previously established (see, for example Frisch, 1995), this scaling is impacted by the internal intermittency of the turbulent dissipation. This is highlighted in Figure 5, which shows some of the structure functions up to $n = 10$ scaled by $n/3$, using the same 1500 m ensembles as used to determine ε. These structure functions exhibit the expected effects of internal intermittency, with constancy only observed for the third order case.

The same structure functions shown in Figure 5 are replotted in Figure 6 with the scaling exponent selected to provide a constant value within the inertial subrange. Note that the lack of statistical convergence becomes amplified at low spatial separations with increasing n, making the selected values of ζ_n increasingly subjective. That said, the estimated exponents are consistent with the values observed from previous studies. This is illustrated in Figure 7, which shows the structure function exponents, ζ_n , as a function of order of the structure function, n, calculated using the 9:04 MDT flight data and compared with previously reported values. The current results are found to be slightly closer to the Kolmogorov (1941) prediction than prior studies, which could reflect an improvement in the estimated exponents due to the data within the inertial subrange being acquired spatially, rather than temporally, as done in previous studies. Alternatively, it could reflect the sensitivity of these results to the level of convergence of the structure function at higher order. Measurement campaigns to acquire additional flight data over a range of stability conditions are currently being conducted.

CONCLUSIONS

Unmanned aerial vehicles have the potential to provide high fidelity vertical profiles of atmospheric boundary layer statistics. Examples presented here from the LAPSE-RATE campaign conducted in the San Luis Valley in Colorado, USA show that they are able to capture complex boundary layer structure, including the presence of multiple stable layers which evolve to adiabatic mixed-layer conditions during a morning transition, the presence of strong horizontal wind shear corresponding to these individual stable layers, and the corresponding turbulent kinetic energy profiles.

The results presented here also demonstrate the potential to obtain high-Reynolds-number turbulence data in the atmospheric boundary layer using unmanned aerial vehicles. As these vehicles are traveling at velocities an order of magnitude faster than the wind velocity, the statistics are effectively being measured in space, rather than time. This capability was employed to capture turbulence spectra with over a decade of resolved inertial subrange, allowing the

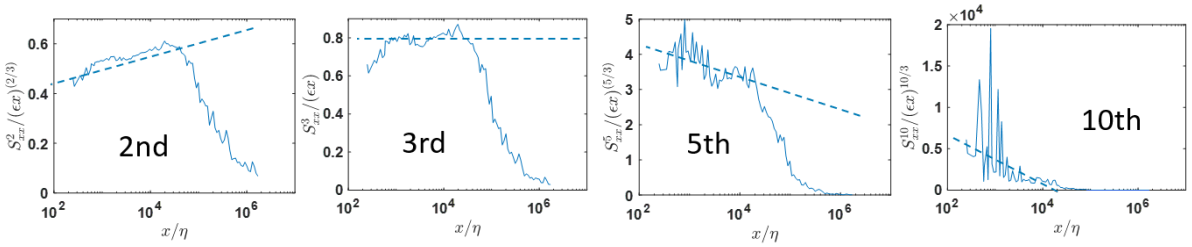

Figure 5. Ensemble-averaged structure functions for $n = 2, 3, 5$ and 10, calculated using the 9:04 MDT flight data. Structure functions shown scaled by $n/3$.

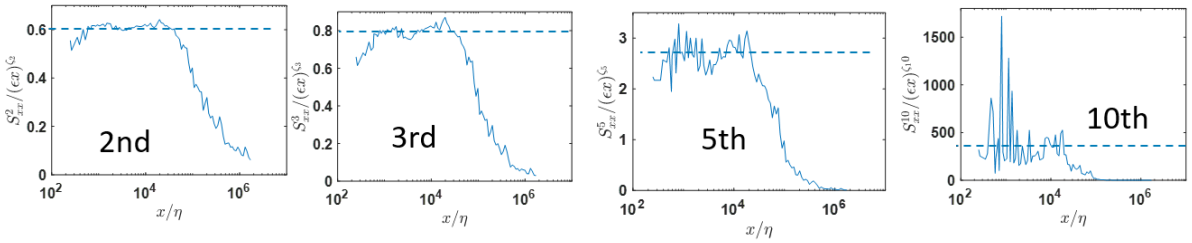

Figure 6. Ensemble-averaged structure functions for $n = 2, 3, 5$ and 10, calculated using the 9:04 MDT flight data. Structure functions shown scaled by ζ_n value selected to provide most constant value within the inertial subrange.

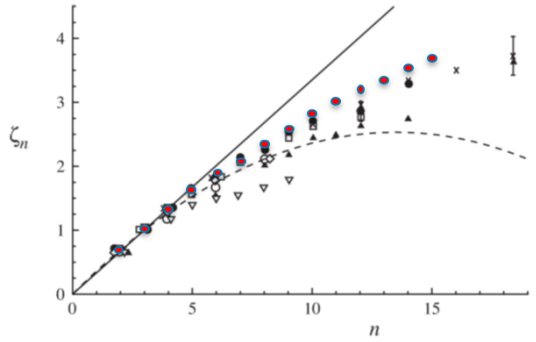

Figure 7. Structure function inertial layer exponents, ζ_n , as a function of order of the structure function, n. Structure function exponents calculated using the 9:04 MDT flight data are shown as red symbols. Solid line is $n/3$, dashed line is refined similarity hypothesis of Kolmogorov (1962), symbols are from Anselmet *et al.* (1984). Adapted from Pope (2000).

assessment of inertial subrange scaling through the calculation of structure functions up to 10th order. Limitations in the approach of using UAVs appear as decreased statistical convergence at longer separation distances, and through the limited frequency response of the five-hole probe. Improvements are currently being made in the measurement system to improve these qualities.

The results presented in this paper were supported by the US National Science Foundation through grant #CBET-1351411 and by US National Science Foundation award #1539070, Collaboration Leading Operational UAS Development for Meteorology and Atmospheric Physics (CLOUDMAP). Funding for LAPSE-RATE leveraged a variety of existing projects with limited general support for LAPSE-RATE provided by the US National Science Foundation (AGS 1807199) in the form of travel support for early career participants. Support for the planning and execution of the campaign was provided by the NOAA Physical Sciences Division and NOAA UAS Program. Finally, the support of UASColorado and local government agencies (Alamosa County, Saguache County) was critical in securing site permissions and other local logistics.

REFERENCES

Anselmet, F., Gagne, Y., Hopfinger, E.J. & Antonia, R.A. 1984 High-order velocity structure functions in turbulent shear flow. *J. Fluid Mech.* **140**, 63–89.

Egger, J., Bajrachaya, S., Heingrich, R., Kolb, P., Lammlein, S., Mech, M., Reuder, J., Schäper, W., Shakya, P., Shween, J. & H., Wendt. 2002 Diurnal winds in the himalayan kali gandaki valley. part iii: Remotely piloted aircraft soundings. *Mon. Wea. Rev.* **130**, 2042–2058.

Elston, Jack, Argrow, Brian, Stachura, Maciej, Weibel, Doug, Lawrence, Dale & Pope, David 2015 Overview of small fixed-wing unmanned aircraft for meteorological sampling. *Journal of Atmospheric and Oceanic Technology* **32** (1), 97–115.

Frisch, U. 1995 *Turbulence: The Legacy of A. N. Kolmogorov*. Cambridge University Press.

Hobbs, S., Dyer, D., Courault, D., Olioso, A., Lagouarde, J.-P., Kerr, Y., McAnneney, J. & Bonnefond, J. 2002 Surface layer profiles of air temperature and humidity measured from unmanned aircraft. *Agronomie* **22** (6), 635–640.

Kolmogorov, A. N. 1941 The local structure of turbulence in incompressible viscous fluid for very large reynolds numbers. *Dokl. Akad. Nauk SSSR* **30**, 301–305.

Kolmogorov, A. N. 1962 A refinement of previous hypotheses concerning the local structure of turbulence in a viscous incompressible fluid at high reynolds number. *Journal of Fluid Mechanics* **13** (1), 8285.

van den Kroonenberg, A., Martin, T., Buschmann, M., Bange, J. & Vörsmann, P. 2008 Measuring the wind vector using the autonomous mini aerial vehicle M^2AV. *J. Atmos. Oceanic Technol.* **25**, 1969–1982.

Lampert, A., Pätzold, F., Jiménez, M. A., Lobitz, L., Martin, S., Lohmann, G., Canut, G., Legain, D., Bange,

J., Martínez-Villagrasa, D. & Cuxart, J. 2016 A study of local turbulence and anisotropy during the afternoon and evening transition with an unmanned aerial system and mesoscale simulation. *Atmospheric Chemistry and Physics* **16** (12), 8009–8021.

Martin, Sabrina, Beyrich, Frank & Bange, Jens 2014 Observing entrainment processes using a small unmanned aerial vehicle: A feasibility study. *Boundary-Layer Meteorology* **150** (3), 449–467.

Perry, A.E., Henbest, S. & Chong, M.S. 1986 A theoretical and experimental study of wall turbulence. *J. Fluid Mech.* **165**, 163–199.

Platis, Andreas, Altstädter, Barbara, Wehner, Birgit, Wildmann, Norman, Lampert, Astrid, Hermann, Markus, Birmili, Wolfram & Bange, Jens 2016 An observational case study on the influence of atmospheric boundary-layer dynamics on new particle formation. *Boundary-Layer Meteorology* **158** (1), 67–92.

Pope, S. B. 2000 *Turbulent Flows*. Cambridge University Press.

Spiess, Thomas, Bange, Jens, Buschmann, Marco & Vörsmann, Peter 2007 First application of the meteorological Mini-UAV 'M2AV'. *Meteorologische Zeitschrift* **16** (2), 159–169.

Taylor, G. I. 1938 The spectrum of turbulence. *Proc. R. Soc. Lond.* **164** (919), 476–490.

Townsend, A. A. 1976 *The Structure of Turbulent Shear Flow*. Cambridge, UK: Cambridge University Press.

Wildmann, Norman, Rau, Gerrit Anke & Bange, Jens 2015 Observations of the early morning boundary-layer transition with small remotely-piloted aircraft. *Boundary-Layer Meteorology* **157** (3), 345–373.

Witte, Brandon M, Singler, Robert F & Bailey, Sean CC 2017 Development of an unmanned aerial vehicle for the measurement of turbulence in the atmospheric boundary layer. *Atmosphere* **8** (10), 195.